

## Large-Grained Cylindrical Block Copolymer Morphologies by One-Step Room-Temperature Casting

Arkadiusz A. Leniart, Przemyslaw Pula, Esther H. R. Tsai, and Pawel W. Majewski\*

Cite This: *Macromolecules* 2020, 53, 11178–11189

Read Online

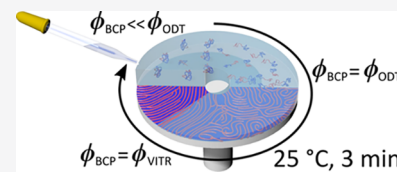
ACCESS |

Metrics & More

Article Recommendations

Supporting Information

**ABSTRACT:** We report a facile method of ordering block copolymer (BCP) morphologies in which the conventional two-step casting and annealing steps are replaced by a single-step process where microphase separation and grain coarsening are seamlessly integrated within the casting protocol. This is achieved by slowing down solvent evaporation during casting by introducing a nonvolatile solvent into the BCP casting solution that effectively prolongs the duration of the grain-growth phase. We demonstrate the utility of this solvent evaporation annealing (SEA) method by producing well-ordered large-molecular-weight BCP thin films in a total processing time shorter than 3 min without resorting to any extra laboratory equipment other than a basic casting device, *i.e.*, spin- or blade-coater. By analyzing the morphologies of the quenched samples, we identify a relatively narrow range of polymer concentration in the wet film, just above the order–disorder concentration, to be critical for obtaining large-grained morphologies. This finding is corroborated by the analysis of the grain-growth kinetics of horizontally oriented cylindrical domains where relatively large growth exponents (1/2) are observed, indicative of a more rapid defect-annihilation mechanism in the concentrated BCP solution than in thermally annealed BCP melts. Furthermore, the analysis of temperature-resolved kinetics data allows us to calculate the Arrhenius activation energy of the grain coarsening in this one-step BCP ordering process.



### INTRODUCTION

The attractiveness of complex nanostructures fabrication *via* macromolecular self-assembly is inherently linked to the simplicity of this approach. Block copolymers (BCPs) are arguably one of the most appealing embodiments of the self-assembling paradigm. Since their discovery, a range of basic and very complex nanoscale BCP morphologies have been reported along with detailed processing protocols.<sup>1</sup> A particularly strong emphasis has been placed on the development of methods such as directed self-assembly (DSA) that harness the random formation of BCP domains, increase grain size, and align (orient) BCP morphologies.<sup>2,3</sup> Over the course of more than 50 years of BCP research, the DSA methods, which stem from uncomplicated solvent casting or thermal annealing, have broadly diversified in terms of the ordering biases that they employ and greatly increased their sophistication level.<sup>3–5</sup> To mention just a few examples, the arsenal of DSA includes methods that employ electric<sup>6–8</sup> and magnetic fields,<sup>9–11</sup> epitaxial patterning,<sup>12–16</sup> laser light,<sup>17–20</sup> and microwaves.<sup>21,22</sup> Unarguably, DSA techniques have helped in the understanding of physics underlying the BCP self-assembly, obtaining more reproducible structures, and exercising better control over the process but at the price of increased complexity. Frequently, the ever-growing demand for better control and the increase in BCP processing technical complexity require expensive instrumentation and impose a starting barrier for researchers who are new to the BCP field. This technical barrier reduces the original appeal of the bottom-up self-assembly strategy.

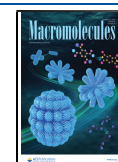
The approach to BCP processing that we present in this work reaches back to very straightforward and well-established protocols of ordering BCP microdomains by slow evaporation of solvent from BCP solutions used in bulk-morphology studies.<sup>23–26</sup> Our method is reduced to a single-step BCP casting from a volatile-nonvolatile solvent mixture by either spin-, blade- or dip-coating, with successive BCP microphase separation and grain growth concomitant with solvent evaporation. As evidenced by our experiments, this approach yields well-ordered, large-grained horizontal morphologies of a relatively large-molecular-weight ( $M_n = 116$  kg/mol) cylinder-forming poly(styrene-*b*-2-vinylpyridine) (PS-*b*-P2VP) directly after the room-temperature (RT) casting, with no further annealing.

The existence of ordered morphologies in BCP solutions above the order–disorder transition concentration ( $\phi_{BCP} > \phi_{ODT}$ ) has been reported for block copolymer solutions and solvent-swollen thin films.<sup>25,27–29</sup> Following the observation by Kim and Libera, who used solvent casting to order a thin-film poly(styrene)-*b*-poly(butadiene)-*b*-poly(styrene) triblock,<sup>26</sup> solvent annealing has been used as an attractive alternative to thermal annealing. Solvent casting and annealing protocols

Received: September 3, 2020

Revised: November 13, 2020

Published: December 1, 2020



have been demonstrated for various BCP systems. Notably, Russell and co-workers have reported the fabrication of well-ordered vertical arrays of hexagonally packed cylinders by spin-casting of poly(styrene-*b*-ethylene oxide) (PS-*b*-PEO) films in benzene vapor atmosphere with the ordering of vertical cylinders driven by the solvent evaporation front.<sup>30</sup> A transition from spherical micelles in solution to cylindrical domains upon direct casting poly(styrene-*b*-4-vinylpyridine) (PS-*b*-P4VP) from tetrahydrofuran (THF) was reported by the same group.<sup>31</sup> A facile approach to BCP membranes ordering utilizing an evaporating solvent front has also been proposed by Phillip et al. who used the immersion method to produce vertically aligned BCP membranes and recognized the critical role of solvent concentration profile developing in the film upon rapid evaporation in nucleation and growth of vertically ordered cylindrical domains in poly(styrene-*b*-lactic acid) (PS-*b*-PLA) membranes.<sup>32</sup> Membranes built of high- $\chi$  materials such as PS-*b*-P4VP with remarkable pore regularity were obtained by casting from solvent mixtures exploiting preferential BCP block–solvent interactions.<sup>29</sup>

Another attractive DSA method that relies on solvent–BCP interactions is solvent vapor annealing (SVA). Originally shown to induce order in roll-cast triblock BCP films,<sup>33</sup> the SVA technique drew a lot of interest in BCP research community and quickly evolved from a simple bell-jar to very advanced automated setups with real-time monitoring of the solvent uptake enabling precise control of the swelling and deswelling ramps.<sup>34–38</sup> In addition, SVA can be coupled with other ordering biases, such as topographically patterned substrates,<sup>39,40</sup> heating,<sup>22,41,42</sup> soft-shearing,<sup>43,44</sup> or dynamic solvent vapor-jet rastering<sup>45</sup> to yield significantly faster ordering and lower defectivity. The SVA approach is particularly effective in annealing large  $M_n$  BCPs, difficult and impractically slow to order with purely thermal methods.<sup>46,47</sup> SVA with a reactive solvent vapor can induce chemical transformations in the film and subsequent morphological reorganization, *e.g.*, acid hydrolysis of protective solketal groups in glycerol monomethacrylate block, leading to a rapid increase in the  $\chi$  parameter and inducing phase separation in a small-pitch BCP.<sup>48</sup> The importance of solvent selection in the casting-step prior to SVA annealing was reported by Gotrik and Ross who observed that less volatile casting solvents, *i.e.*, providing less free volume, increased the degree of ordering of bilayered cylindrical poly(styrene-*b*-dimethylsiloxane) (PS-*b*-PDMS) in the subsequent SVA-thermal quench experiments.<sup>40</sup> Similarly, the selection of the casting method could determine the final BCP morphology; Zhang et al. demonstrated the role of residual stresses in blade-coated cylindrical poly(styrene-*b*-methyl methacrylate) (PS-*b*-PMMA) in vertical orientation of the BCP domains during the subsequent thermal annealing.<sup>49</sup>

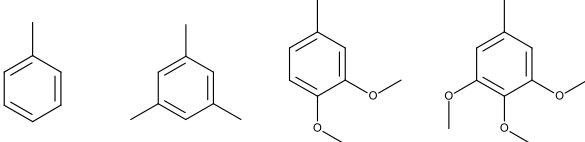
The interactions between the polymer and a poor or marginal solvent are used in another post-casting BCP ordering method called immersion annealing (IA). The degree of BCP swelling and thus the degree of plasticization can be controlled by the selection of the composition of the binary solvent mixture in the immersion bath. Karim et al. used this approach to induce long-range order in PS-*b*-PMMA and PS-*b*-P2VP BCP films immersed in the mixtures of good and marginal solvents.<sup>50</sup> A similar approach has been used by Jung and co-workers who optimized temperature and composition of a solvent–nonsolvent immersion bath to rapidly order high- $\chi$  PS-*b*-PDMS material in graphoepitaxial trench patterns.<sup>51</sup>

Multistep SVA annealing combined with IA in a solvent mixture proposed by Choi and co-workers has been shown to induce morphological transition in sphere-forming PS-*b*-PDMS diblock and to be a much more rapid annealing method than the conventional one-step SVA.<sup>52</sup>

Frequently, SVA experiments require very precise temperature control as the polymer swelling/deswelling equilibrium is extremely sensitive to temperature and vapor pressure changes.<sup>53</sup> Although it is possible to further accelerate the grain growth of BCP in solvent vapor annealing by combining it with thermal treatment,<sup>21,22,54</sup> due to the strong coupling between the temperature and solvent vapor–liquid equilibrium, at elevated substrate temperatures, the solvent favors the gas-phase shifting the equilibrium toward the polymer deswelling. Conversely, the decrease in film's temperature with respect to the solvent's reservoir induces a steep BCP swelling with the associated risk of crossing the critical solvent uptake and the order–disorder transition concentration ( $\varphi_{ODT}$ ) or reaching the dew point and vapor condensation followed by a rapid dewetting of the film.<sup>53</sup> Moreover, the degree of swelling and the rate of deswelling strongly influence the BCP microphase separation pathway and the resulting ordered morphologies. For example, solvent removal rate at the end of SVA experiment has been demonstrated to determine the orientation of cylinder-forming poly(styrene-*b*-isoprene-*b*-styrene) triblock copolymer,<sup>55</sup> cylinder-gyroid phase selection and domains' orientation in PS-*b*-PLA,<sup>56</sup> sphere packing in asymmetric PS-*b*-P4VP,<sup>28</sup> and the relative in- and out-of-plane defectivity in lamellae-forming P2VP-*b*-PS-*b*-P2VP triblock.<sup>37</sup>

The selection of a proper solvent or solvent mixture composition is critical in solvent-driven DSA methods outlined above. Its role is not only plasticization of the system by lowering the glass-transition temperature and increasing chain diffusivity but also affecting the chemical interactions between the BCP blocks.<sup>28,34,57,58</sup> BCP dilution with near-neutral solvent lowers the chemical incompatibility between the blocks ( $\chi_{eff}$ ) and decreases the Flory–Huggins segmental interaction parameter ( $\chi_{AB}$ ):  $\chi_{eff} = \chi_{AB} \cdot \varphi^\beta$ , with scaling exponent  $\beta$  assuming values 1.3–1.6 in the modified dilution approximation model.<sup>59,60</sup> Activated diffusion of BCP chains steeply increases with  $\chi$  parameter reduction in accordance with  $\langle D \rangle \sim D_0 \exp^{-\alpha \chi N_A}$ , where  $D_0$  is the self-diffusion coefficient in a hypothetical phase-mixed system,  $N_A$  is the number of segments of the minority block in an asymmetric BCP, and  $\alpha$  is a constant ( $\alpha \approx 1$ ).<sup>53,61</sup> The interaction parameter  $\chi$  influences the system's morphology both in the solution<sup>62</sup> and in the swollen state during the SVA experiments.<sup>28,57,63</sup> Ober et al. have shown that the morphology of poly( $\alpha$ -methylstyrene)-*b*-poly(4-hydroxystyrene) can be switched from cylindrical to spherical by sequential exposure to nonselective and block-selective solvent vapor.<sup>64</sup> Remarkable control of the BCP morphology can be achieved by providing not only in- and out-of-plane periodicity tunability,<sup>36,65</sup> but also, with the use of selective solvent, a selection of characteristic morphology.<sup>66,67</sup>

Casting polymers from solvent mixtures, used to control the evaporation rate of solvent from the drying films, has been recognized as a viable method of improving internal order in these materials, *e.g.*, casting semiconducting polythiophenes from a mixture of volatile (*e.g.*, chloroform, chlorobenzene) and less volatile cosolvent (*e.g.*, di- or trichlorobenzene), increases the degree of crystallinity as well as the size of the crystalline domains by extending the nucleation and growth phase.<sup>68,69</sup> Mechanistically, binary mixture casting bears

Table 1. Physical Properties and Hansen Solubility Parameters of the Solvents Used in This Study<sup>76–80</sup>


	Toluene	1,3,5-trimethylbenzene	3,4-dimethoxytoluene	3,4,5-trimethoxytoluene
Density [g cm <sup>-3</sup> ]	0.87	0.86	1.05	1.08
Boiling point [°C]	111	165	220 <sup>76</sup>	273 <sup>77</sup>
Vapor pressure [mmHg]	26 <sup>78</sup>	2.49 <sup>79</sup>	0.17 <sup>76</sup>	0.01 <sup>77</sup>
Hansen solubility parameter ( $\delta$ ) [MPa <sup>1/2</sup> ]	18.3 <sup>80</sup>	15.4	18.7	19.4

resemblance to solvent vapor annealing, taking advantage of retention of nonvolatile solvent what increases chain diffusivity during the film drying. The beneficial role of residual volatile solvent in block copolymer film ordering has been reported by Perego and co-workers who quantitatively described the role of entrapped toluene in the acceleration of domain coarsening kinetics in thermally annealed PS-*b*-PMMA thin films.<sup>70,71</sup> Recently, the direct casting approach utilizing delayed solvent evaporation was employed by Gu and co-workers who successfully used chloronaphthalene and 1-methylnaphthalene mixtures with toluene as a host solvent to produce well-ordered, large-area PS-*b*-P2VP cylindrical morphologies in a roll-to-roll fabrication process.<sup>72</sup> In the same report, the researchers have utilized a nonvolatile dibutyl phthalate plasticizer for PS-*b*-PEO ordering. This method proved very effective; however, immersion in an ethanol bath was necessary to rinse the plasticizer at the end of the process. Jung et al. have combined nonvolatile solvent spin-casting with *in situ* heating with a high-power IR lamp to evaporate diphenyl and dibenzyl ethers to order lamellar PS-*b*-PMMA without the need for neutral-brush grafting typically required for obtaining vertically oriented BCP lamellae.<sup>73</sup>

## RESULTS

The effectiveness of single-step solvent evaporation annealing (SEA), as assessed by the extent of the lateral ordering of horizontally oriented cylindrical PS-*b*-P2VP with a total molecular weight of 116 kg/mol (C116), hinges critically on the selection of the casting solvent. We searched for nonvolatile compounds, liquid at room temperature and characterized by neutral or near-neutral interaction parameter with the diblock. We have selected three different solvents, 1,3,5-trimethylbenzene (mesitylene, Mes), 3,4-dimethoxytoluene (DMOT), and 3,4,5-trimethoxytoluene (TMOT), whose room-temperature vapor pressure, densities, and calculated Hansen interaction parameters ( $\delta_T$ ) are listed in Table 1. In the calculation of  $\delta_T$  for these compounds, we followed the protocol proposed by Panayiotou.<sup>74,75</sup> The calculation details of the dispersive, hydrogen-bonding, and polar contributions to the Hansen solubility parameters, along with the calculated

Flory–Huggins solvent–BCP block interaction parameters are provided in the Supporting Information.

**Spin-to-Dry Casting.** Rather than directly dissolving the BCP in pure nonvolatile solvents what would lead to very slow evaporation rates during casting and potentially require a major modification of the casting protocols, we diluted the selected compounds with a much more volatile solvent, toluene, commonly used in the BCP research. The advantage of using the binary mixture of nonvolatile and volatile solvents is twofold: (i) the volatile solvent helps in the coating process by greatly improving macroscopic film quality, (ii) the evaporation of the more volatile solvent defines the wet-film thickness at the early stages of the coating process allowing direct use of the previously established spin- or blade-coating protocols, *i.e.*, without the need of any auxiliary equipment such as heaters.<sup>73</sup> For the latter reason, in this experimental series, we used a standard room-temperature spin-coating protocol (0.8 wt % polymer solution, 2000 rpm), and varied only the composition of the casting solvent mixture. The first of the tested compounds—mesitylene ( $p_{0, 25^\circ\text{C}} = 2.5$  mmHg) used in 1:9 Mes/Tol mass ratio ( $\approx 10$  vol %), despite its good compatibility with the coating process, *i.e.*, providing high-quality, smooth films, has not yielded large-grained BCP morphologies (Figure S1b). We observed only short, poorly ordered micelles with grain size,  $\xi$ , quantified here by the characteristic decay length of the image autocorrelation function calculated from the scanning electron microscopy (SEM) maps of the azimuthal orientation of BCP domains,<sup>81</sup> smaller than the cylinder-to-cylinder distance ( $L_0$ ). Notably, the extent of microphase separation is more advanced than in the case of neat toluene casting (Figure S1a). This encouraging result indicates the importance of solvent retention and film drying rate (*ca.* 1000 nm/s for Tol<sup>82</sup> vs 200 nm/s for Mes) on the grain coarsening process. By replacing Mes with less volatile DMOT ( $p_{0, 25^\circ\text{C}} = 0.17$  mmHg), we slowed down the evaporation of solvent during the BCP ordering phase to 4.1 nm/s. Figure 1 shows the utility of our method in ordering cylindrical PS-*b*-P2VP material spin-cast from DMOT/Tol (1:9 mixture) at a constant velocity (2000 rpm) performed at room temperature (23 °C). As indicated by the *in situ* spectral reflectance measurements (Figure 1a), the entire casting and

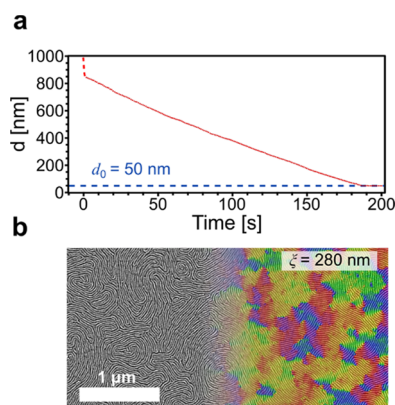


**Figure 1.** Single-step casting and ordering of C116 PS-*b*-P2VP performed at room temperature using the spin-to-dry method, *i.e.*, annealing directly on a rotating (2000 rpm) spin-coater chuck. (a) Wet-film thickness evolution during spin-coating of 0.8 wt % C116 solution cast from the 1:9 DMOT/Tol mixture. (b) SEM of the resulting morphology with a false-color grain orientation map. Total processing time  $\approx 3$  min.

annealing process takes only 180 s to complete. After this very rapid processing, a surprisingly large-grained morphology forms with grain size,  $\xi \approx 230 \pm 50$  nm. The degree of order in the film is in stark contrast with the results of vacuum oven annealing of this material where only poorly ordered vertical cylinders were observed after 16 h of annealing at 200 °C (Figure S1c) and is comparable to the size of grains observed after  $\sim 1$  h long annealing experiments of SVA in THF vapor reported by Gu *et al.* for a lower  $M_n$  (90 kg/mol) cylindrical PS-*b*-P2VP homolog.<sup>27</sup> As anticipated, using a very low vapor pressure cosolvent, TMOT ( $p_{0,25^\circ\text{C}} = 0.01$  mmHg) in place of DMOT slows down the overall film drying rate even further (1.4 nm/s, spin-to-dry time  $\approx 600$  s), and results in larger grains,  $\xi \approx 310 \pm 40$  nm (Figure S2).

A heuristic approach to the optimization of this one-step BCP ordering process in terms of increasing the BCP grain size would suggest increasing the concentration of the less volatile solvent mixture component. Interestingly, after increasing the DMOT/toluene ratio to 1:4, the BCP grain size averages at  $\xi \approx 278 \pm 50$  nm. This marginal increase is related to a small increase in the spin-to-dry time (200 s) resulting from a slower drying rate (3.5 nm/s). Surprisingly, an increase in nonvolatile DMOT content (1:1 DMOT/toluene) does not lead to a further decrease in the film drying rate. However, since the evaporation rate is one of the factors defining the thickness of the wet films in the spin-coating process,<sup>83</sup> the films cast from less volatile solvents are generally thinner than their more volatile, *e.g.*, toluene-cast, counterparts. At 1:1 DMOT/Tol ratio, the utilization of the same protocol (0.8%, 2000 rpm) still yields horizontally oriented domains but only partially covering the substrate. For similar reasons, using the single-step casting and ordering approach with neat DMOT or TMOT solutions would be impractical (spin-to-dry time is increased to  $>20$  min at RT). Also, for casting mixtures with the initial TMOT concentration of 20% (1:4 TMOT/toluene ratio), the drying process in the spin-coater chamber takes  $>20$  min and the BCP film was nonhomogeneous, with reticular morphology regions (Figure S3), indicating the need for adjustment of the spin-coating conditions. We concluded that for the room-temperature spin-to-dry casting of 0.8 wt % BCP solution from the mixture of DMOT and toluene, the

moderate DMOT concentration ( $\approx 20$  vol %), and 2000 rpm spin speed are optimal in terms of resulting films' quality and allow sufficient time for self-assembly and BCP ordering.

**Phase Transitions Induced by Solvent Evaporation.** The single-step casting and ordering experiment can be schematically divided into three parts as shown in Figure 2.

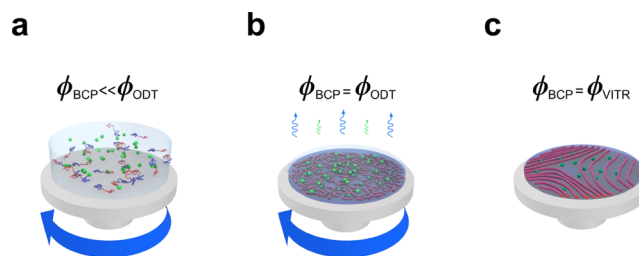


**Figure 2.** Schematic representation of transitions occurring during BCP casting from a mixture of nonvolatile and volatile solvents. (a) After the initial wet-film thickness is established, rapid evaporation of the volatile solvent from the disordered BCP solution induces a transition to an ordered BCP solution (b) when the critical, order-disorder polymer concentration is reached. (c) BCP morphology evolution continues until the system vitrifies. The less volatile solvent molecules depicted as green balls dominate during the late-stage of the casting and ordering (b, c).

In the first part, during the spin-off, the inertia and viscous forces dominate causing the rapid outflow of the polymer solution from the substrate and  $\sim 1$   $\mu\text{m}$  film thickness is reached within the first 1–2 s of the process (red dashed line in Figure 1a).<sup>83</sup> The composition of the coating solution, *i.e.*, the BCP and less volatile solvent concentrations are not significantly altered at this point.

The solvents continue to evaporate and the concentration of BCP ( $\phi_{\text{BCP}}$ ) increases, at some point reaching the critical value of the solvent-driven order-disorder phase transition ( $\phi_{\text{ODT}}$ ) and the onset of formation of the ordered microphase-separated morphology.<sup>84</sup> If the process is continued, the wet-film thickness is further decreasing, until the polymer chain vitrifies ( $\phi_{\text{vitr}}$ ) and the final dry-film thickness is reached ( $\phi = 1$ ). As depicted in Figure 2b,c, the time interval between the two final steps ( $\phi_{\text{ODT}} < \phi < \phi_{\text{BCP}}$ ) is the location of the BCP domains coarsening. The rates at which the two solvents evaporate from the film are not equal. While the partial pressure of each component of the mixture is proportional to its molar fraction in solution as approximated by the Raoult's law ( $p_i = x_i p_{0i}$ , where  $x_i$  is the molar fraction of a component,  $p_{0i}$  is the vapor pressure of the pure component), the total vapor pressure of the mixture which determines the evaporation rate of the mixture is the sum of the two. We have investigated the evolution of the composition of DMOT- and TMOT-toluene mixtures during evaporation at room temperature by tracking it with <sup>1</sup>H NMR spectroscopy. Figure 3 shows that over the course of evaporation, reported here as a decrease in the overall weight of the binary solvent mixture, the solution is enriched in the less volatile component. For the starting composition of DMOT/toluene and TMOT/toluene mixtures of 1:4 (weight ratios), after evaporation of 70% of the mixture weight, the weight proportions are 2:1 and 3:1 ( $\approx 67$  vol % DMOT and  $\approx 75$  vol % TMOT), respectively, and the less volatile components dominate. Under an approximate assumption that the wet 1  $\mu\text{m}$  thick film loses  $\approx 95\%$  of the solvent before reaching the final dry state, we conclude that the

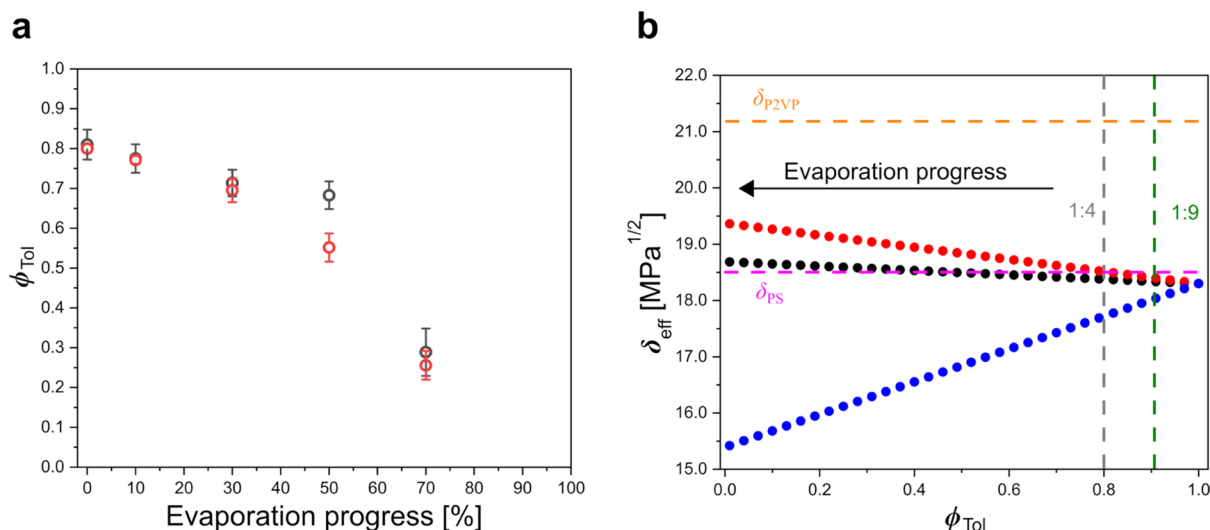


**Figure 3.** Composition evolution of the BCP casting mixtures during evaporation at room temperature. (a) The concentration of the more volatile component, toluene, rapidly decreases from the initial volume fraction of approximately 80% (1:4 weight ratio) in both the DMOT/Tol and TMOT/Tol mixtures. The experimental data were derived from <sup>1</sup>H NMR analysis, and the associated error bars indicate measurement uncertainties. (b) The calculated effective Hansen solubility parameter changes in the progress of toluene evaporation as the mixture becomes rich in the less volatile components. The vertical dashed lines indicate the initial composition of the casting mixture used in this study. The horizontal dashed lines indicate the Hansen solubility parameter of P2VP (orange) and PS (pink), respectively.<sup>80,85</sup> The black, red, and blue symbols mark DMOT/Tol, TMOT/Tol, and Mes/Tol mixtures, respectively.

final, grain growth enabling step of BCP self-assembly takes place in TMOT- or DMOT-rich environment. It is worth noting that the fast evaporation of toluene is, in part, responsible for the relatively weak dependence of the total spin-to-dry time on the initial concentration of the less volatile component in the casting solution.

The change in the mixture composition is accompanied by the progressive evolution of the effective Hansen solubility parameter of the mixture. In both cases,  $\delta_{\text{T}}$  increases as the mixture becomes toluene-lean (Figure 3b) due to the increased concentration of DMOT and TMOT whose polar methoxy groups increase the polar and hydrogen-bonding contributions to the total Hansen parameter (Table S3). Therefore, in the domain growth enabling concentration range, the mixture's solvency becomes somewhat more preferential for the P2VP block than the initial casting mixture. Similarly, the effective solvent–BCP block interaction parameter evolves toward a lower degree of incompatibility with the P2VP block. Table S7 in the Supporting Information contains the calculated enthalpic contributions to the Flory–Huggins interaction parameters for P2VP and PS in pure DMOT, TMOT, and in their mixtures with toluene.<sup>63</sup> Interestingly, Hansen solubility parameter decreases as toluene evaporates from mesitylene/toluene mixtures decreasing the preferential interactions with the more polar P2VP block which might, additionally, contribute to the poor BCP ordering observed with this solvent (Figure 3b).

**Quench Experiments.** To investigate the final stages of the simultaneous casting-and-ordering process responsible for grain coarsening, we performed an experiment during which the drying wet-film morphology was quenched at various thicknesses by rapid solvent evaporation. The quench can be accomplished by a rapid temperature increase<sup>40</sup> or, as in this case, by a decrease of the ambient pressure under isothermal conditions. In particular, we wanted to identify the onset of BCP grain coarsening, *i.e.*, the minimal concentration of the polymer in the solvent mixture which displays microphase-

separated morphologies, and the concentration region over which the process of grain coarsening takes place. We prepared a series of wet samples by interrupting the spin-coating process when the thickness of the wet film reached  $\approx 500$  nm. At the corresponding BCP concentration ( $\approx 10$  vol %), the polymeric solution is still homogeneous. The wet samples were transferred into a thermostated chamber equipped with a removable lid and allowed us to continue drying at room temperature under the natural convection conditions (significantly slower than on the rotating spin-coating chuck). Their thickness was monitored with the optical reflectometer and, once the wet film thickness reached a certain value, the chamber was closed and rapidly evacuated to  $\sim 1$  mbar causing immediate evaporation of the solvent. The morphology of the quenched samples was investigated by SEM. In Figure 4 the grain size is plotted as a function of the polymer concentration at the start of the quench experiment. The samples which were

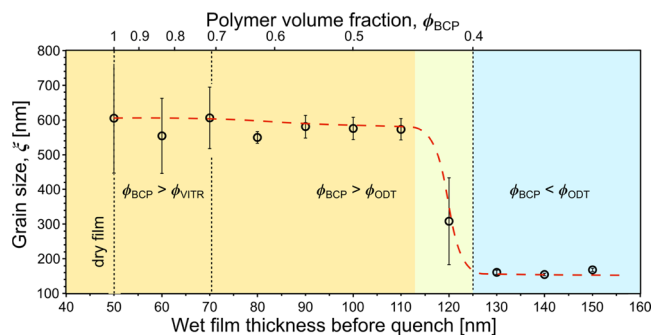


**Figure 4.** Grain size in vacuum-quenched C116 samples while drying at 0.6 nm/s at room temperature. The approximate locations of rapid domain's coarsening and slower growth are marked in light green and yellow, respectively. The disordered polymer solution is marked in blue. The black dashed lines at  $\phi_{\text{BCP}} = 1$ ,  $\approx 0.70$ , and  $\approx 0.40$  indicate dry, vitrified, and disordered films, respectively. The red dashed line is a guide to the eye.

quenched below the critical BCP concentration in the film ( $\phi_{\text{BCP}} < 0.4$ ) exhibit very small grain size. It has to be noted, however, that in contrast to the films cast from neat toluene or less volatile mesitylene which are more disordered, the samples display small-grained horizontal cylinders morphology ( $\xi \approx 150$  nm). At the threshold concentration, a long-range order develops rapidly and for the films quenched at 120 nm ( $\phi_{\text{BCP}} = 0.42$ ), the grain size averages 300 nm and broadly varies (standard deviation (SD) = 120 nm) not only in different samples but also in different regions on the same sample, indicating a microscopic heterogeneity of the ordered-phase nucleation and domain growth progress. We emphasize that the effective grain coarsening time in these transitional samples was very short (*ca.* 10 s), yet the resulting grain size is comparable to that of the spun-to-dry samples indicating the importance of the BCP concentration window just below  $\phi_{\text{ODT}}$  in the ordering.

The large grain-size variation was not found in the samples quenched at the later stages (drier films) which present only a small increase in grain size for  $0.45 < \phi < 0.70$  and plateau for  $\phi > 0.70$ .

Our findings are in good agreement with the reports by researchers who studied BCP ordering in SVA experiments. Baruth et al. have identified a narrow solvent concentration window,  $\phi_{\text{THF}} = 0.54\text{--}0.57$  ( $\phi_{\text{BCP}} = 0.43\text{--}0.46$ ), just on the ordered side of the ODT region ( $\phi_{\text{BCP}} = 0.32\text{--}0.40$ ), to be most effective in lateral ordering of vertical domains of cylinder-forming PS-*b*-PLA materials ( $M_n = 63\text{--}104$  kg/mol).<sup>38</sup> Conversely, performing SVA above the critical solvent concentration is ineffective as it induces ODT and erases the sample's processing history.<sup>38,86</sup> In a quantitative *in situ* grazing-incidence small-angle X-ray scattering (GISAXS) study, Russell and co-workers investigated near-neutral solvent swelling of cylindrical PS-*b*-P2VP thin film ( $M_n = 90$  kg/mol) by GISAXS and reported  $\phi_{\text{ODT}} = 0.343$  ( $t/t_{\text{dry}} = 2.92$ ) and  $\phi_{\text{vitr}} = 0.71$  ( $t/t_{\text{wet}} = 1.41$ ) for solvent-driven ODT and vitrification, respectively. At  $\phi = 0.71$  the authors observed the restriction in chain rearrangement due to the proximity of the glass transition and only very slow lateral ordering kinetics resulting in small grains in films annealed above this polymer concentration.<sup>58</sup> The same authors provided the ODT-extrapolated grain-size value ( $\xi_{\text{ODT}}$ ) for a 1-h long SVA experiment performed at 23 °C to be  $\approx 1.9$   $\mu\text{m}$ . This value reported as  $g(r) = 0.5 \cdot g_0$ , somewhat more stringent than  $g(r) = 1/e \cdot g_0$  used here, is of the same order as the largest grain size observed in our study ( $\xi \approx 1.5$   $\mu\text{m}$ ) in C116 films cast from DMOT/Tol mixture at 25 °C in which the evaporation of the solvents was slowed down by placing a cap with an orifice over the drying film (Figure 5). The effective ordering time was  $t \approx 100$  s in this case. Most likely, the increased time-efficiency of the SEA method stems from the early stages of ordering commencing right at the onset of the ODT.

**Grain Coarsening Kinetics.** The increased grain size in samples which were quenched closer to the dry state indicates the significant role of BCP residence in the solvent-swollen state (*i.e.*,  $\phi_{\text{vitr}} < \phi < \phi_{\text{ODT}}$ ) in the growth of large grains. To study the grain coarsening kinetics we searched for a reliable method to control the duration of that time. In principle, the rate of evaporation is affected by (at least) three orthogonal factors: (i) temperature, (ii) ambient pressure, and (iii) the rate of convective removal of the solvent vapor. The evaporation at different ambient pressures provides isothermal ordering conditions but the results of an experiment in which

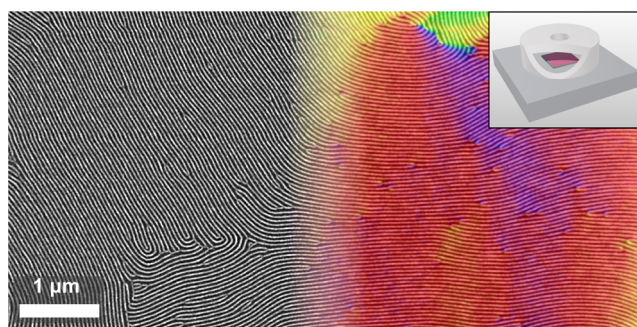


**Figure 5.** Exceptionally large-grained ( $\xi \approx 1.5$   $\mu\text{m}$ ) film in a sample cast from the 1:4 DMOT/Tol mixture whose evaporation at 25 °C was slowed down to 0.1 nm/s by application of a convection-limiting cap with 5 mm orifice (Figure S5). The right-hand side of the image is false-colored to reflect grains orientation. The inset shows the schematics of the evaporation cap. Poly(2-vinylpyridine) domains were converted to an  $\text{Al}_2\text{O}_3$  replica before the SEM imaging.

wet films were dried inside a vacuum chamber evacuated to various pressure levels were only partially satisfactory due to the technical difficulties in adjusting the proper vacuum level. The volume of our vacuum chamber ( $\approx 500$   $\text{cm}^3$ ) was too small to allow complete evaporation of DMOT/Tol mixture at the intermediate pressure levels (100–1000 mbar) and a low flow of nitrogen had to be introduced to facilitate drying of the wet films by the advective outflow of solvent vapors from the chamber.

Temperature variation is arguably the easiest method of controlling the evaporation rate. Due to the exponential dependence of the equilibrium vapor pressure,  $p$  on temperature:  $p \sim p_0 \exp(\text{const} - \Delta H/RT)$  ( $\Delta H$  and  $R$  are the specific enthalpy of vaporization and the gas constant, respectively), even a small change in temperature affects the evaporation rate. We investigated the influence of temperature on the self-assembly of S2VP C116 by employing a procedure similar to the one used in the quench experiments. We interrupted the spin-coating run, placed the wet samples ( $t_{\text{wet}} \approx 500$  nm,  $\phi_{\text{BCP}} \approx 0.1$ ) on a thermostated plate, and allowed the solvent to evaporate completely. The drying rates can be further decreased or increased by placing convection-limiting “caps” on top of the sample or introducing a convective flow of inert gas ( $\text{N}_2$ ), respectively. The caps, which allow *in situ* thickness monitoring are very effective in obtaining large-grained samples. As shown in Figure 5, solvent evaporation through the cap with a 5 mm orifice slows down the drying rate at 25 °C to 0.1 nm/s yielding  $\xi > 1.5$   $\mu\text{m}$ . Conversely, the stream of nitrogen can increase the evaporation rate to 6 nm/s.

The BCP grain coarsening process can be quantitatively described by the kinetic equation

$$\xi = A \exp(-E_a/RT) \cdot t^\alpha$$

where  $E_a$  is the activation barrier in the Arrhenius temperature-dependent term and  $\alpha$  is the kinetic power-law exponent of the time-dependent term.<sup>50,87–89</sup>

To decouple the time and temperature influence, we performed a series of experiments in which we removed the solvents from the wet spun-cast films at different rates under isothermal conditions. By employing the caps with adequately selected orifice diameter or, conversely, by adjusting the flow of the inert gas over the sample, we were able to control the evaporation rate ( $R$ ) of the 1:4 DMOT/Tol mixture between 0.1 nm/s (25 °C) and 21 nm/s (45 °C) (Table S2) providing

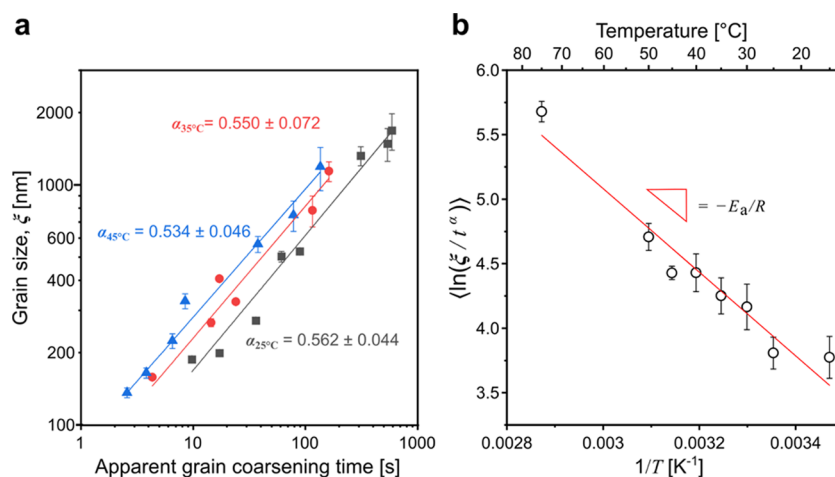


**Figure 6.** Kinetics of grain development in the direct casting of C116 from 1:4 DMOT/Tol mixture assessed by SEM image analysis. (a) Evolution of the grain size (horizontal cylinders) as a function of the apparent coarsening time for three distinct temperatures: 25 °C (black squares), 35 °C (red circles), and 45 °C (blue triangles). The data were fitted to a power law—continuous lines. The error bars represent the standard deviation obtained by analyzing different film regions. (b) Temperature dependence of average grain size after accounting for the coarsening time influence presented in the Arrhenius convention with a linear fit shown in red. The poly(2-vinylpyridine) domains were converted to  $\text{Al}_2\text{O}_3$  replica before the GISAXS study.

more than two decades of variation in the grain coarsening times. Figure 6a shows the kinetics data derived from SEM analysis of C116 morphologies cast at three distinct temperatures—25, 35, and 45 °C. For the lack of precise information on the exact width of the grain coarsening thickness window, we conservatively reported the apparent grain coarsening time ( $t$ ) as the interval between  $\varphi_{\text{ODT}}$  and  $\varphi_{\text{vitr}}$  ( $t = (d_{\text{ODT}} - d_{\text{vitr}})/R$ ). We note, however, that these apparent times can be as much as 3–4× longer than the actual grain-growth times. The power-law exponents ( $\alpha_{25^\circ\text{C}} = 0.562 \pm 0.044$ ,  $\alpha_{35^\circ\text{C}} = 0.550 \pm 0.072$ ,  $\alpha_{45^\circ\text{C}} = 0.534 \pm 0.046$ ) are significantly larger than those found for thermally annealed neat diblock melts of horizontal PS-*b*-PMMA cylinders ( $M_n = 48$  kg/mol) thermally annealed in a vacuum oven ( $\alpha = 0.14$ ), processed with a focused laser beam ( $\alpha = 0.21$ ),<sup>3,88</sup> or by the direct immersion annealing (DIA) (0.17).<sup>50</sup> These values, however, are close to those recently reported by Seguíni and co-workers ( $\alpha \approx 0.5$ ) for vertical 39 kg/mol PS-*b*-PMMA annealed in the intermediate-segregation limit, close to the order–disorder transition,<sup>90</sup> and to those observed by Perego et al. for lamellar-pattern coarsening in the presence of residual solvent trapped in the film ( $\alpha \approx 0.33$ ) annealed by rapid IR-heating.<sup>70</sup> The pre-exponential factors,  $\xi_0$  ( $\xi = \xi_0 t^\alpha$ ), which reflect the grain-growth rates at the early stage of morphology evolution<sup>50</sup> are relatively small:  $\xi_{0, 25^\circ\text{C}} = 46 \pm 12$  nm,  $\xi_{0, 35^\circ\text{C}} = 65 \pm 22$  nm, and  $\xi_{0, 45^\circ\text{C}} = 82 \pm 17$  nm, compared to the thermal (116 nm),<sup>88</sup> laser (255 nm),<sup>88</sup> or direct immersion annealing (122 nm).<sup>50</sup> It is likely, however, that the values of  $\xi_0$  obtained in our analysis are underestimated due to the conservative choice of the apparent grain coarsening times. An additional correction would further shorten the effective coarsening times at higher temperatures to reflect the shift in the onset of the ordered formation toward higher BCP concentrations. For block copolymers in a neutral solvent, the observed ODT (the ordering onset) strongly depends on polymer concentration ( $\chi_{\text{ODT}} \sim 1/T_{\text{ODT}} \sim \varphi_{\text{BCP}}^{-\beta}$  with  $\beta = 1.3$ –1.6), in accordance with the modified mean-field dilution approximation.<sup>60</sup>

BCP grain size values and coarsening kinetics data can be inferred from small-angle X-ray scattering data by application

of the Scherrer formula relating the scattering peak width in the reciprocal space and the grain size in the real space

$$\xi = \frac{2\pi K}{\Delta q}$$

where  $K$  is a dimensionless shape factor ( $\approx 1$ ) and  $\Delta q$  is the peak full width at half-maximum parameter in reciprocal units.<sup>91</sup> We collected a series of synchrotron grazing-incidence small-angle X-ray scattering (GISAXS) patterns on samples previously measured by the SEM. Figure 7a shows an example of such pattern acquired at 0.12° incident angle, with up to fourth-order scattering peaks resolvable, indicating a high degree of positional and orientational order of the cylindrical domains in the samples evaporating over 130 s at 25 °C. The evolution of grain size inferred from the Scherrer analysis is

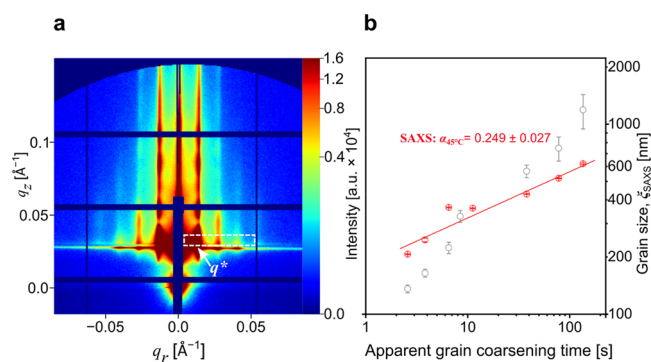


**Figure 7.** (a) Two-dimensional (2D) GISAXS pattern of C116 ordered in 130 s by casting from 1:4 DMOT/Tol mixture at 25 °C collected at a 0.12° beam-incidence angle. (b) Evolution of grain size in films cast at 45 °C (red circles) calculated using the Scherrer formula from the breadth of the primary scattering peak at  $q^* = 0.0125 \text{ \AA}^{-1}$ . For comparison, grain-size values derived from SEM image analysis are represented by gray circles. The red line is the fit to a power law. Poly(2-vinylpyridine) blocks were converted to  $\text{Al}_2\text{O}_3$  replica before the GISAXS experiment. The white dashed line in (a) outlines the region used for GISAXS data integration in the Scherrer grain-size analysis.

shown in Figure 7b. For comparison, we plotted them together with  $\xi$  values obtained from SEM imaging. The GISAXS  $\xi$  values (*i.e.*, in-plane decorrelation lengths of the periodic order) follow a similar trend to the SEM grain-size values. At smaller values, there is a nearly constant ratio between them; however, the two measures diverge at longer coarsening times, with GISAXS  $\xi$  values smaller. In effect, the GISAXS grain-size time scaling exponent ( $\approx 0.25$ ) is smaller than that from the SEM data. To understand this discrepancy, we first accounted for instrumental corrections,<sup>91</sup> which limit the Scherrer method resolution in the large-grained, well-ordered samples. The magnitude of this correction is rather small, indicating that the measured  $\xi$  values are within the beamline resolution limit ( $\approx 1.5 \mu\text{m}$ , Supporting Information). It is important to note that the measures of grain size computed from SEM and GISAXS probe slightly different aspects of ordering. The reported SEM grain-size values are by construction sensitive to decorrelation in orientational order (including grain boundaries and local spread of microdomains orientation), whereas GISAXS-derived  $\xi$  values are additionally affected by positional disorder, *e.g.*, repeat-spacing distribution, dislocations, and line-edge roughness defects.<sup>3</sup> As a result, SEM and GISAXS measurements probe two distinct aspects of sample long-range ordering.<sup>92</sup> The presented data suggest that the orientational order of cylindrical domains (probed by SEM) grows more easily and more quickly than their positional order (*i.e.*, perfect registry) of the periodic morphology. Put otherwise, the orientational order (to which both techniques are sensitive) might initially dominate SAXS measurements to be later overwhelmed by the other peak broadening contributions. Furthermore, it is worth noting that while the measured coarsening trends are robust, the exact values reported depend on the definition of the metrics; *e.g.*, the choice of how to quantify the decay length of the image autocorrelation function and the shape factor in Scherrer analysis.

Utilizing the SEM data, we calculated the activation energy of the grain coarsening process, following the approach used by Modi *et al.* who used it to analyze the results of the direct immersion annealing experiments.<sup>50</sup> In Figure 6b, we plotted the averaged values of  $\xi$  normalized by the time factors for different temperatures in the Arrhenius plot convention (*i.e.*, ensemble-averaged  $\ln(\xi/t^\alpha)$  vs  $1/T$ ) and extracted the activation energy of grain coarsening:  $E_a = 26.9 \pm 2.7$  kJ/mol. This value is significantly lower than the activation energy  $E_a = 270$  kJ/mol obtained for thermal annealing of horizontal cylindrical PS-*b*-PMMA pattern ( $M_n = 63$  kg/mol),<sup>87</sup> and DIA ( $E_a = 111 \pm 63$  kJ/mol).<sup>50</sup> It can qualitatively be explained by lowering the energetic cost of polymer chain mixing, *i.e.*, lowering the effective  $\chi$  parameter in the presence of solvent and increasing chain diffusivity.<sup>27,53,93</sup> This result is also consistent with the results of a comparative study of PS-*b*-P2VP solvent and thermal annealing close to the ODT which indicated that faster chain diffusion in SVA results in much larger BCP grains.<sup>58</sup> Additionally, lowering  $\chi_{\text{eff}}$  accelerates the ordering by lowering the activation barrier of defects annihilation along the free-energy pathway between defective and ordered states.<sup>94</sup>

We realize that the analysis of the SEA grain coarsening kinetics data presented in our report is based on several simplifying assumptions. Some of them, like the overestimation of the coarsening time duration, can be relatively easily accounted for after more precise localization of the BCP ordering regime (*e.g.*, by an *in situ* GISAXS study). Other

factors and dependencies were purposefully omitted in our analysis to allow a direct comparison of SEA with other DSA methods. For example, the time scaling exponents were assumed to be constant in the evaporative annealing series performed at a constant temperature. We note, however, that a more advanced analysis model could include an intricate dependency of  $\alpha$  on the BCP concentration and the effective Flory–Huggins interaction parameter,  $\chi_{\text{eff}}$  following the trend similar to the one reported for vertical BCP pattern coarsening:  $\alpha \sim \exp(-\chi \cdot N_A)$ .<sup>95</sup> In the case of SEA, using the modified-dilution approximation:  $\alpha \sim \exp(-\chi_{\text{eff}} N_A) = \exp(-\chi_{\text{AB}} \varphi^{-\beta} \cdot N_A)$ , the generalized kinetics equation would have the following form:  $\xi = A \exp(-E_a(\varphi)/RT) \cdot t^{\alpha(\varphi)}$ , with  $\alpha$  being concentration- and, thus, time-dependent. A proposed solution to deconvolve these dependencies is to perform a technically challenging SEA experiment at a constant BCP concentration, *i.e.*, a time study at a series of wet-film thickness isochores. Analogous to the constant-swelling-ratio SVA study reported by Gu *et al.*,<sup>58</sup> such experiments may, in principle, be performed by exercising precise control over the solvent pressure above the swollen film,<sup>35</sup> or by retention of nonvolatile plasticizer as proposed by Weller and co-workers.<sup>72</sup>

## CONCLUSIONS

Overall, our straightforward, single-step solvent evaporation annealing protocol is a viable alternative to more complex block-copolymer directed self-assembly methods. Due to its simplicity and compatibility with various film-casting techniques, the method is easy to implement in any soft-matter research laboratory, enabling rapid BCP patterning on various substrates without the need for specialized processing instrumentation. As such, it could be an attractive choice for investigators outside of the BCP research community who would like to study these self-assembling materials. Moreover, due to the exceptionally short BCP processing duration (*ca.* 100 s), SEA might be attractive for commercial applications. The reported grain coarsening data indicate that the method can be further optimized in terms of both obtaining larger grain size and shortening the processing time. While the former can potentially be achieved by increasing the film drying temperature and limiting the convection, the latter requires a deeper insight into the BCP ordering and grain-growth phenomena near the solvent evaporation induced order–disorder phase transition. In particular, as indicated by the quench experiments, the early stages of ordered-morphology formation, just above the  $\varphi_{\text{ODT}}$ , are expected to be the most valuable in terms of fast grain-growth kinetics due to the high diffusivity of BCP chains. Shortening the total processing time is therefore possible by a rapid spin-down followed by a dwell in a relatively narrow processing window optimal for obtaining large BCP grains, analogous to time-effective SVA protocols.<sup>38,58</sup> A similar strategy has been proposed for other self-assembling systems, *e.g.*, in the alignment of liquid crystalline BCPs which respond to magnetic fields only in a narrow temperature-enabled kinetic window.<sup>96</sup> In SVA, which in large part resembles the direct casting method, as pointed out by Lundy *et al.*, the characteristic time of phase separation decreases very steeply with the degree of solvent supersaturation,<sup>53</sup> emphasizing the importance of precise control of solvent vapor pressure in the dynamic equilibrium with the swollen film available in the advanced annealing setups.<sup>35</sup> Finally, the last stage, direct casting, *i.e.*, the transition from dynamically evolving to a



vitrified state, is likely important for the resulting BCP morphology analogously to the SVA experiments in which the rate of solvent removal is critical for the preservation of the ordered structure and, in the limiting cases, can be disrupted upon drying.<sup>36,37,97</sup>

## METHODS

**Materials.** A series of BCP solutions were prepared by dissolving cylinder-forming polystyrene-*block*-poly(2-vinylpyridine) (S2VP C116, 79 kg/mol-*b*-36.5 kg/mol, polydispersity index (PDI) = 1.05, Polymer Source, Inc.) in binary mixtures of toluene (GPC grade, Carl Roth) with less volatile solvents—1,3,5-trimethylbenzene (mesitylene, 98%, Sigma-Aldrich), 3,4-dimethoxytoluene (DMOT, 96%, Sigma-Aldrich), and 3,4,5-trimethoxytoluene (TMOT, 97%, Sigma-Aldrich). The less volatile solvents were mixed with toluene at 1:9, 1:4, and 1:1 cosolvent/toluene weight ratios, while the concentration of S2VP C116 was kept constant at 0.8 wt % with respect to the total mass of the solvent mixture.

**Single-Step Spin-to-Dry Experiments.** Block copolymer thin films were spin-cast onto 15 × 15 mm<sup>2</sup>, 0.5 mm thick silicon wafers cleaned by oxygen plasma (PE-25, Plasma Etch, 150 mTorr O<sub>2</sub>, 100 W RF power, 120 s). The spin-casting protocol in the spin-to-dry experiments started with deposition of 50 μL of 0.8 wt % BCP solution on a stationary substrate followed by spinning at a constant velocity (2000 rpm) until the thickness of the film monitored with an optical reflectometer (F-20, Filmetrics) has reached a stable, dry-state value (~50 nm). In the case of the 1:4 DMOT/Tol solvent mixture, the solvents evaporate in ~200 s. To produce wet films, the spin-coating was stopped when the film thickness has reached ~500 nm, and before all solvent has evaporated, by rapidly decelerating the chuck at ~2000 rpm/s. The spin-coater (SPIN 150i, SPS) was operated at room temperature (23 °C) under a gentle flow of nitrogen (~2 L/min) delivered to the coater chamber (~4.5 L) through the motor-shaft assembly and venting to the atmosphere through a central circular opening (diameter, ~50 mm) in a splash-protection lid.

**Quench Experiments.** In the quench experiments, wet BCP films (~500 nm thick) were placed inside a thermostated (25 °C) chamber with a removable vacuum lid and allowed drying under ambient conditions. The drying process was monitored by the spectral reflectometer and, after the desired film thickness was reached, the vacuum lid was closed and the chamber was evacuated to 1 mbar, resulting in instantaneous (~1 s) evaporation of the solvent.

**Evaporation at Various Temperatures.** In the evaporation-temperature series, the wet BCP samples were transferred onto a large thermal mass aluminum block whose temperature was controlled by a circulating water bath (CC-K6s, Huber) in the range from 15 to 75 °C and allowed evaporating under natural or under forced convection conditions induced by a flow of N<sub>2</sub>. To obtain long evaporation times, the convection was slowed down by placing low-profile aluminum caps with orifices over the drying samples. The lowest temperature employed was limited by the dew point of water vapor (12 °C) at the relative humidity of 50% at 23 °C.

**Microscopy and Image Analysis.** SEM imaging contrast was improved by selective conversion of P2VP domains to Al<sub>2</sub>O<sub>3</sub> replica by three cycles of sequential exposure to trimethylaluminum and water vapors carried out at 85 °C in a home-built sequential infiltration synthesis<sup>98</sup> reactor with a base pressure of ~2 Torr. After the removal of organics by oxygen plasma, the samples were examined under the field emission SEM (FE-SEM) (Zeiss, Merlin) operating at 2 keV with an in-lens detector of secondary electrons. The SEM-derived grain-size values were reported here as the characteristic decay length of the autocorrelation function of the horizontal domains orientation  $g(r)$ , obtained by fitting  $g(r)$  to an exponential function  $e^{-r/\xi}$  using Python-written routines from the SciAnalysis package.<sup>81</sup> All of the reported  $\xi$  values are the average of three to five individual measurements performed on 12 × 8 μm<sup>2</sup> images collected within the central 8 mm × 8 mm sample region. The error bars represent the standard deviation (SD) of the mean  $\xi$  values.

**GISAXS.** Synchrotron grazing-incidence small-angle X-ray scattering (GISAXS) experiments were performed at the 11-BM Complex Materials Scattering (CMS) beamline of the National Synchrotron Light Source II at Brookhaven National Laboratory. Two-dimensional scattering images were collected using a hybrid pixel-array detector (Dectris Pilatus 2M) located 5 m downstream from the sample. GISAXS patterns of the BCP samples on Si substrates (15 × 8 mm<sup>2</sup>) were acquired across a range of incidence angles (0.08–0.14°) in the air using an X-ray beam of  $\lambda = 0.9184$  Å. Silver behenate powder was used as a  $q$ -value calibration standard. The X-ray beam (50 μm high × 200 μm wide) at 0.12° angle of incidence illuminated a rectangular region (~2 mm<sup>2</sup>) near the center-line of the substrate. To ensure that sample edge effects (*i.e.*, the spin-coating edge beading artifacts) are eliminated, ~1 mm of the polymer film near the substrate edge was removed. The in-plane correlation length (“SAXS grain size”) was estimated using the Scherrer peak width analysis, after accounting for instrumental peak broadening contribution. The reported  $\xi$  values are the average of measurements performed on three individual patterns collected at distinct locations near the sample’s center-line. The error bars represent the standard deviation of the mean  $\xi$  values.

## ASSOCIATED CONTENT

### Supporting Information

The Supporting Information is available free of charge at <https://pubs.acs.org/doi/10.1021/acs.macromol.0c02026>.

Wet-film drying rates, large-scale SEM images of well-ordered BCP morphologies, blade- and dip-coating protocols with SEM images of the coated samples, description of the NMR analysis of solvent mixture composition, and calculation of Hansen solubility parameters and GISAXS Scherrer grain size (PDF)

## AUTHOR INFORMATION

### Corresponding Author

Pawel W. Majewski — Department of Chemistry, University of Warsaw, Warsaw 02089, Poland; [orcid.org/0000-0001-6338-2411](https://orcid.org/0000-0001-6338-2411); Email: [pmajewski@chem.uw.edu.pl](mailto:pmajewski@chem.uw.edu.pl)

### Authors

Arkadiusz A. Leniart — Department of Chemistry, University of Warsaw, Warsaw 02089, Poland; [orcid.org/0000-0001-6629-6383](https://orcid.org/0000-0001-6629-6383)

Przemyslaw Pula — Department of Chemistry, University of Warsaw, Warsaw 02089, Poland

Esther H. R. Tsai — Center for Functional Nanomaterials, Brookhaven National Laboratory, Upton, New York 11973, United States

Complete contact information is available at:

<https://pubs.acs.org/10.1021/acs.macromol.0c02026>

### Author Contributions

A.A.L. and P.W.M. discovered the effect and conceived the plan of the study. A.A.L. carried out the experiments and associated research, including sample preparation, processing, and SEM characterization. P.W.M. and P.P. assisted in experimental aspects. P.P. calculated Hansen solubility parameters of solvents used in this study. E.H.R.T. performed GISAXS measurements and contributed to GISAXS data analysis. P.W.M. interpreted and performed the quantitative analysis of the kinetics data. All authors contributed to the manuscript text and content.

### Notes

The authors declare no competing financial interest.

## ACKNOWLEDGMENTS

The authors gratefully acknowledge Dr. Kevin Yager's help with GISAXS data analysis, his input in the CMS beamline automation, and the development of SEM/SAXS data processing routines.<sup>81</sup> A.A.L., P.P., and P.W.M. acknowledge financial support from the First Team program (POIR.04.04.00-00-1DE6/16) of the Foundation for Polish Science co-financed by the European Union under the European Regional Development Fund. This research used beamline 11-BM (CMS) of the National Synchrotron Light Source II and the Center for Functional Nanomaterials (CFN), both of which are U.S. Department of Energy (DOE) Office of Science User Facilities operated for the DOE Office of Science by Brookhaven National Laboratory under Contract no. DE-SC0012704.

## REFERENCES

- (1) Bates, C. M.; Bates, F. S. 50th Anniversary Perspective: Block Polymers—Pure Potential. *Macromolecules* **2017**, *50*, 3–22.
- (2) Hu, H.; Gopinadhan, M.; Osuji, C. O. Directed Self-Assembly of Block Copolymers: A Tutorial Review of Strategies for Enabling Nanotechnology with Soft Matter. *Soft Matter* **2014**, *10*, 3867–3889.
- (3) Majewski, P. W.; Yager, K. G. Rapid Ordering of Block Copolymer Thin Films. *J. Phys.: Condens. Matter* **2016**, *28*, No. 403002.
- (4) Darling, S. B. Directing the Self-Assembly of Block Copolymers. *Prog. Polym. Sci.* **2007**, *32*, 1152–1204.
- (5) Li, W.; Müller, M. Directed Self-Assembly of Block Copolymers by Chemical or Topographical Guiding Patterns: Optimizing Molecular Architecture, Thin-Film Properties, and Kinetics. *Prog. Polym. Sci.* **2016**, *54–55*, 47–75.
- (6) Xu, T.; Zvelindovsky, A. V.; Sevinck, G. J. A.; Lyakhova, K. S.; Jinnai, H.; Russell, T. P. Electric Field Alignment of Asymmetric Diblock Copolymer Thin Films. *Macromolecules* **2005**, *38*, 10788–10798.
- (7) Liedel, C.; Pester, C. W.; Ruppel, M.; Urban, V. S.; Böker, A. Beyond Orientation: The Impact of Electric Fields on Block Copolymers. *Macromol. Chem. Phys.* **2012**, *213*, 259–269.
- (8) Park, M. J.; Balsara, N. P. Anisotropic Proton Conduction in Aligned Block Copolymer Electrolyte Membranes at Equilibrium with Humid Air. *Macromolecules* **2010**, *43*, 292–298.
- (9) Tao, Y.; Zohar, H.; Olsen, B. D.; Segalman, R. A. Hierarchical Nanostructure Control in Rod-Coil Block Copolymers with Magnetic Fields. *Nano Lett.* **2007**, *7*, 2742–2746.
- (10) Gopinadhan, M.; Majewski, P. W.; Beach, E. S.; Osuji, C. O. Magnetic Field Alignment of a Diblock Copolymer Using a Supramolecular Route. *ACS Macro Lett.* **2012**, *1*, 184–189.
- (11) Majewski, P. W.; Gopinadhan, M.; Osuji, C. O. Magnetic Field Alignment of Block Copolymers and Polymer Nanocomposites: Scalable Microstructure Control in Functional Soft Materials. *J. Polym. Sci., Part B: Polym. Phys.* **2012**, *50*, 2–8.
- (12) Bitá, I.; Yang, J. K. W.; Yeon, S. J.; Ross, C. A.; Thomas, E. L.; Berggren, K. K. Graphoepitaxy of Self-Assembled Block Copolymers on Two-Dimensional Periodic Patterned Templates. *Science* **2008**, *321*, 939–943.
- (13) Kim, S. O.; Solak, H. H.; Stoykovich, M. P.; Ferrier, N. J.; De Pablo, J. J.; Nealey, P. F. Epitaxial Self-Assembly of Block Copolymers on Lithographically Defined Nanopatterned Substrates. *Nature* **2003**, *424*, 411–414.
- (14) Stoykovich, M. P.; Nealey, P. F. Block Copolymers and Conventional Lithography. *Mater. Today* **2006**, *9*, 20–29.
- (15) Albert, J. N. L.; Baney, M. J.; Stafford, C. M.; Kelly, J. Y.; Epps, T. H. Generation of Monolayer Gradients in Surface Energy and Surface Chemistry for Block Copolymer Thin Film Studies. *ACS Nano* **2009**, *3*, 3977–3986.
- (16) Gunkel, I. Directing Block Copolymer Self-Assembly on Patterned Substrates. *Small* **2018**, *14*, No. 1802872.
- (17) Tan, K. W.; Wiesner, U. Block Copolymer Self-Assembly Directed Hierarchically Structured Materials from Nonequilibrium Transient Laser Heating. *Macromolecules* **2019**, *52*, 395–409.
- (18) Jin, H. M.; Lee, S. H.; Kim, J. Y.; Son, S. W.; Kim, B. H.; Lee, H. K.; Mun, J. H.; Cha, S. K.; Kim, J. S.; Nealey, P. F.; Lee, K. J.; Kim, S. O. Laser Writing Block Copolymer Self-Assembly on Graphene Light-Absorbing Layer. *ACS Nano* **2016**, *10*, 3435–3442.
- (19) Leniart, A. A.; Pula, P.; Sitkiewicz, A.; Majewski, P. W. Macroscopic Alignment of Block Copolymers on Silicon Substrates by Laser Annealing. *ACS Nano* **2020**, *14*, 4805–4815.
- (20) Singer, J. P.; Lin, P. T.; Kooi, S. E.; Kimerling, L. C.; Michel, J.; Thomas, E. L. Direct-Write Thermocapillary Dewetting of Polymer Thin Films by a Laser-Induced Thermal Gradient. *Adv. Mater.* **2013**, *25*, 6100–6105.
- (21) Zhang, X.; Harris, K. D.; Wu, N. L. Y.; Murphy, J. N.; Buriak, J. M. Fast Assembly of Ordered Block Copolymer Nanostructures through Microwave Annealing. *ACS Nano* **2010**, *4*, 7021–7029.
- (22) Jin, C.; Murphy, J. N.; Harris, K. D.; Buriak, J. M. Deconvoluting the Mechanism of Microwave Annealing of Block Copolymer Thin Films. *ACS Nano* **2014**, *8*, 3979–3991.
- (23) Inoue, T.; Soen, T.; Hashimoto, T.; Kawai, H. Thermodynamic Interpretation of Domain Structure in Solvent-Cast Films of A-B Type Block Copolymers of Styrene and Isoprene. *J. Polym. Sci., Part A-2: Polym. Phys.* **1969**, *7*, 1283–1302.
- (24) Shibayama, M.; Hashimoto, T.; Hasegawa, H.; Kawai, H. Ordered Structure in Block Polymer Solutions. 3. Concentration Dependence of Microdomains in Nonselective Solvents. *Macromolecules* **1983**, *16*, 1427–1433.
- (25) Bates, F. S.; Berney, C. V.; Cohen, R. E. Microphase Structure of Solvent-Cast Diblock Copolymers and Copolymer-Homopolymer Blends Containing Spherical Microdomains. *Macromolecules* **1983**, *16*, 1101–1108.
- (26) Kim, G.; Libera, M. Kinetic Constraints on the Development of Surface Microstructure in SBS Thin Films. *Macromolecules* **1998**, *31*, 2670–2672.
- (27) Gu, X.; Gunkel, I.; Hexemer, A.; Gu, W.; Russell, T. P. An In Situ Grazing Incidence X-Ray Scattering Study of Block Copolymer Thin Films During Solvent Vapor Annealing. *Adv. Mater.* **2014**, *26*, 273–281.
- (28) Gunkel, I.; Gu, X.; Sun, Z.; Schaible, E.; Hexemer, A.; Russell, T. P. An In Situ GISAXS Study of Selective Solvent Vapor Annealing in Thin Block Copolymer Films: Symmetry Breaking of In-Plane Sphere Order upon Deswelling. *J. Polym. Sci., Part B: Polym. Phys.* **2016**, *54*, 331–338.
- (29) Marques, D. S.; Vainio, U.; Chaparro, N. M.; Calo, V. M.; Bezahd, A. R.; Pitera, J. W.; Peinemann, K. V.; Nunes, S. P. Self-Assembly in Casting Solutions of Block Copolymer Membranes. *Soft Matter* **2013**, *9*, 5557–5564.
- (30) Kim, S. H.; Misner, M. J.; Xu, T.; Kimura, M.; Russell, T. P. Highly Oriented and Ordered Arrays from Block Copolymers via Solvent Evaporation. *Adv. Mater.* **2004**, *16*, 226–231.
- (31) Park, S.; Wang, J.-Y.; Kim, B.; Chen, W.; Russell, T. P. Solvent-Induced Transition from Micelles in Solution to Cylindrical Microdomains in Diblock Copolymer Thin Films. *Macromolecules* **2007**, *40*, 9059–9063.
- (32) Phillip, W. A.; Hillmyer, M. A.; Cussler, E. L. Cylinder Orientation Mechanism in Block Copolymer Thin Films upon Solvent Evaporation. *Macromolecules* **2010**, *43*, 7763–7770.
- (33) Albalak, R. J.; Capel, M. S.; Thomas, E. L. Solvent Swelling of Roll-Cast Triblock Copolymer Films. *Polymer* **1998**, *39*, 1647–1656.
- (34) Sinturel, C.; Vayer, M.; Morris, M.; Hillmyer, M. A. Solvent Vapor Annealing of Block Polymer Thin Films. *Macromolecules* **2013**, *46*, 5399–5415.
- (35) Hulkkonen, H.; Salminen, T.; Niemi, T. Automated Solvent Vapor Annealing with Nanometer Scale Control of Film Swelling for Block Copolymer Thin Films. *Soft Matter* **2019**, *15*, 7909–7917.
- (36) Bai, W.; Yager, K. G.; Ross, C. A. In Situ Characterization of the Self-Assembly of a Polystyrene–Polydimethylsiloxane Block

Copolymer during Solvent Vapor Annealing. *Macromolecules* **2015**, *48*, 8574–8584.

(37) Sun, Z.; Russell, T. P. In Situ Grazing Incidence Small-Angle X-Ray Scattering Study of Solvent Vapor Annealing in Lamellae-Forming Block Copolymer Thin Films: Trade-off of Defects in Deswelling. *J. Polym. Sci., Part B: Polym. Phys.* **2017**, *55*, 980–989.

(38) Baruth, A.; Seo, M.; Lin, C. H.; Walster, K.; Shankar, A.; Hillmyer, M. A.; Leighton, C. Optimization of Long-Range Order in Solvent Vapor Annealed Poly(styrene)-block-poly(lactide) Thin Films for Nanolithography. *ACS Appl. Mater. Interfaces* **2014**, *6*, 13770–13781.

(39) Park, S.; Kim, B.; Yavuzcetin, O.; Tuominen, M. T.; Russell, T. P. Ordering of PS-*b*-P4VP on Patterned Silicon Surfaces. *ACS Nano* **2008**, *2*, 1363–1370.

(40) Gotrik, K. W.; Ross, C. A. Solvothermal Annealing of Block Copolymer Thin Films. *Nano Lett.* **2013**, *13*, S117–S122.

(41) Yu, X.; Han, Y. Thermal and Solvent Annealing of Block Copolymer Films. In *Directed Self-Assembly of Block Co-polymers for Nano-manufacturing*; Gronheid, R.; Nealey, P., Eds.; Woodhead Publishing: Cambridge, Waltham, Kidlington, 2015; pp 47–66.

(42) Singer, J. P.; Gotrik, K. W.; Lee, J. H.; Kooi, S. E.; Ross, C. A.; Thomas, E. L. Alignment and Reordering of a Block Copolymer by Solvent-Enhanced Thermal Laser Direct Write. *Polymer* **2014**, *55*, 1875–1882.

(43) Luo, M.; Scott, D. M.; Epps, T. H. Writing Highly Ordered Macroscopic Patterns in Cylindrical Block Polymer Thin Films via Raster Solvent Vapor Annealing and Soft Shear. *ACS Macro Lett.* **2015**, *4*, 516–520.

(44) Qiang, Z.; Zhang, Y.; Groff, J. A.; Cavicchi, K. A.; Vogt, B. D. A Generalized Method for Alignment of Block Copolymer Films: Solvent Vapor Annealing with Soft Shear. *Soft Matter* **2014**, *10*, 6068–6076.

(45) Seppala, J. E.; Lewis, R. L.; Epps, T. H. Spatial and Orientation Control of Cylindrical Nanostructures in ABA Triblock Copolymer Thin Films by Raster Solvent Vapor Annealing. *ACS Nano* **2012**, *6*, 9855–9862.

(46) Kim, E.; Ahn, H.; Park, S.; Lee, H.; Lee, M.; Lee, S.; Kim, T.; Kwak, E.-A.; Lee, J. H.; Lei, X.; Huh, J.; Bang, J.; Lee, B.; Ryu, D. Y. Directed Assembly of High Molecular Weight Block Copolymers: Highly Ordered Line Patterns of Perpendicularly Oriented Lamellae with Large Periods. *ACS Nano* **2013**, *7*, 1952–1960.

(47) Doerk, G. S.; Li, R.; Fukuto, M.; Yager, K. G. Wet Brush Homopolymers as “Smart Solvents” for Rapid, Large Period Block Copolymer Thin Film Self-Assembly. *Macromolecules* **2020**, *53*, 1098–1113.

(48) Yu, D. M.; Smith, D. M.; Kim, H.; Mapas, J. K. D.; Rzaev, J.; Russell, T. P. Morphological Evolution of Poly(solketal methacrylate)-block-polystyrene Copolymers in Thin Films. *Macromolecules* **2019**, *52*, 3592–3600.

(49) Zhang, X.; Douglas, J. F.; Jones, R. L. Influence of Film Casting Method on Block Copolymer Ordering in Thin Films. *Soft Matter* **2012**, *8*, 4980–4987.

(50) Modi, A.; Bhaway, S. M.; Vogt, B. D.; Douglas, J. F.; Al-Enizi, A.; Elzatahry, A.; Sharma, A.; Karim, A. Direct Immersion Annealing of Thin Block Copolymer Films. *ACS Appl. Mater. Interfaces* **2015**, *7*, 21639–21645.

(51) Park, W. I.; Kim, J. M.; Jeong, J. W.; Jung, Y. S. Deep-Nanoscale Pattern Engineering by Immersion-Induced Self-Assembly. *ACS Nano* **2014**, *8*, 10009–10018.

(52) Choi, Y. J.; Byun, M. H.; Park, T. W.; Choi, S.; Bang, J.; Jung, H.; Cho, J.-H.; Kwon, S.-H.; Kim, K. H.; Park, W. I. Rapid and Cyclable Morphology Transition of High- $\chi$  Block Copolymers via Solvent Vapor-Immersion Annealing for Nanoscale Lithography. *ACS Appl. Nano Mater.* **2019**, *2*, 1294–1301.

(53) Lundy, R.; Flynn, S. P.; Cummins, C.; Kelleher, S. M.; Collins, M. N.; Dalton, E.; Daniels, S.; Morris, M. A.; Enright, R. Controlled Solvent Vapor Annealing of a High  $\chi$  Block Copolymer Thin Film. *Phys. Chem. Chem. Phys.* **2017**, *19*, 2805–2815.

(54) Cummins, C.; Mokarian-Tabari, P.; Andrezza, P.; Sinturel, C.; Morris, M. A. Solvothermal Vapor Annealing of Lamellar Poly(styrene)-block-poly(d,l-lactide) Block Copolymer Thin Films for Directed Self-Assembly Application. *ACS Appl. Mater. Interfaces* **2016**, *8*, 8295–8304.

(55) Albert, J. N. L.; Young, W.-S.; Lewis, R. L.; Bogart, T. D.; Smith, J. R.; Epps, T. H. Systematic Study on the Effect of Solvent Removal Rate on the Morphology of Solvent Vapor Annealed ABA Triblock Copolymer Thin Films. *ACS Nano* **2012**, *6*, 459–466.

(56) Wu, Y.-H.; Lo, T.-Y.; She, M.-S.; Ho, R.-M. Morphological Evolution of Gyroid-Forming Block Copolymer Thin Films with Varying Solvent Evaporation Rate. *ACS Appl. Mater. Interfaces* **2015**, *7*, 16536–16547.

(57) Ghoshal, T.; Chaudhari, A.; Cummins, C.; Shaw, M. T.; Holmes, J. D.; Morris, M. A. Morphological Evolution of Lamellar Forming Polystyrene-block-poly(4-vinylpyridine) Copolymers under Solvent Annealing. *Soft Matter* **2016**, *12*, 5429–5437.

(58) Gu, X.; Gunkel, I.; Hexemer, A.; Russell, T. P. Controlling Domain Spacing and Grain Size in Cylindrical Block Copolymer Thin Films by Means of Thermal and Solvent Vapor Annealing. *Macromolecules* **2016**, *49*, 3373–3381.

(59) Lodge, T. P.; Pan, C.; Jin, X.; Liu, Z.; Zhao, J.; Maurer, W. W.; Bates, F. S. Failure of the Dilution Approximation in Block Copolymer Solutions. *J. Polym. Sci., Part B: Polym. Phys.* **1995**, *33*, 2289–2293.

(60) Lodge, T. P.; Hanley, K. J.; Pudil, B.; Alahapperuma, V. Phase Behavior of Block Copolymers in a Neutral Solvent. *Macromolecules* **2003**, *36*, 816–822.

(61) Yokoyama, H.; Kramer, E. J. Self-Diffusion of Asymmetric Diblock Copolymers with a Spherical Domain Structure. *Macromolecules* **1998**, *31*, 7871–7876.

(62) Park, S.-Y.; Sul, W.-H.; Chang, Y.-J. A Study on the Selectivity of Toluene/Ethanol Mixtures on the Micellar and Ordered Structures of Poly(styrene-*b*-4-vinylpyridine) Using Small-Angle X-Ray Scattering, Generalized Indirect Fourier Transform, and Transmission Electron Microscopy. *Macromolecules* **2007**, *40*, 3757–3764.

(63) O'Driscoll, S.; Demirel, G.; Farrell, R. A.; Fitzgerald, T. G.; O'Mahony, C.; Holmes, J. D.; Morris, M. A. The Morphology and Structure of PS-*b*-P4VP Block Copolymer Films by Solvent Annealing: Effect of the Solvent Parameter. *Polym. Adv. Technol.* **2011**, *22*, 915–923.

(64) Bosworth, J. K.; Black, C. T.; Ober, C. K. Selective Area Control of Self-Assembled Pattern Architecture Using a Lithographically Patternable Block Copolymer. *ACS Nano* **2009**, *3*, 1761–1766.

(65) Jung, Y. S.; Ross, C. A. Solvent-Vapor-Induced Tunability of Self-Assembled Block Copolymer Patterns. *Adv. Mater.* **2009**, *21*, 2540–2545.

(66) Park, W. I.; Tong, S.; Liu, Y.; Jung, I. W.; Roelofs, A.; Hong, S. Tunable and Rapid Self-Assembly of Block Copolymers Using Mixed Solvent Vapors. *Nanoscale* **2014**, *6*, 15216–15221.

(67) Gotrik, K. W.; Hannon, A. F.; Son, J. G.; Keller, B.; Alexander-Katz, A.; Ross, C. A. Morphology Control in Block Copolymer Films Using Mixed Solvent Vapors. *ACS Nano* **2012**, *6*, 8052–8059.

(68) Gu, X.; Reinspach, J.; Worfolk, B. J.; Diao, Y.; Zhou, Y.; Yan, H.; Gu, K.; Mannsfeld, S.; Toney, M. F.; Bao, Z. Compact Roll-to-Roll Coater for in Situ X-Ray Diffraction Characterization of Organic Electronics Printing. *ACS Appl. Mater. Interfaces* **2016**, *8*, 1687–1694.

(69) Liu, J.; Zeng, S.; Jing, P.; Zhao, K.; Liang, Q. Investigating the Effect of Cosolvents on P3HT/O-IDTBR Film-Forming Kinetics and Film Morphology. *J. Energy Chem.* **2020**, *51*, 333–341.

(70) Perego, M.; Ferrarese Lupi, F.; Ceresoli, M.; Giammaria, T. J.; Seguíni, G.; Enrico, E.; Boarino, L.; Antonioli, D.; Gianotti, V.; Sparnacci, K.; Laus, M. Ordering Dynamics in Symmetric PS-*b*-PMMA Diblock Copolymer Thin Films during Rapid Thermal Processing. *J. Mater. Chem. C* **2014**, *2*, 6655–6664.

(71) Sparnacci, K.; Chiarcos, R.; Gianotti, V.; Laus, M.; Giammaria, T. J.; Perego, M.; Munaò, G.; Milano, G.; De Nicola, A.; Haese, M.; Kreuzer, L. P.; Widmann, T.; Müller-Buschbaum, P. Effect of Trapped

Solvent on the Interface between PS-*b*-PMMA Thin Films and P(S-*r*-MMA) Brush Layers. *ACS Appl. Mater. Interfaces* **2020**, *12*, 7777–7787.

(72) Weller, D. W.; Galuska, L.; Wang, W.; Ehlenburg, D.; Hong, K.; Gu, X. Roll-to-Roll Scalable Production of Ordered Microdomains through Nonvolatile Additive Solvent Annealing of Block Copolymers. *Macromolecules* **2019**, *52*, 5026–5032.

(73) Jung, H.; Woo, S.; Choe, Y.; Ryu, D. Y.; Huh, J.; Bang, J. Single Step Process for Self-Assembled Block Copolymer Patterns via in Situ Annealing during Spin-Casting. *ACS Macro Lett.* **2015**, *4*, 656–660.

(74) Stefanis, E.; Panayiotou, C. Prediction of Hansen Solubility Parameters with a New Group-Contribution Method. *Int. J. Thermophys.* **2008**, *29*, 568–585.

(75) Venkatram, S.; Kim, C.; Chandrasekaran, A.; Ramprasad, R. Critical Assessment of the Hildebrand and Hansen Solubility Parameters for Polymers. *J. Chem. Inf. Model.* **2019**, *59*, 4188–4194.

(76) 3,4-Dimethoxytoluene. <http://www.thegoodscentscompany.com/data/rw1183611.html> (accessed Jul 28, 2020).

(77) 3,4,5-Trimethoxytoluene. <http://www.thegoodscentscompany.com/data/rw1182721.html> (accessed Jul 28, 2020).

(78) Toluene. <https://www.sigmaaldrich.com/catalog/product/sial/244511> (accessed Jul 28, 2020).

(79) 1,3,5-Trimethylbenzene. <https://www.sigmaaldrich.com/catalog/product/supelco/442236> (accessed Jul 28, 2020).

(80) Barton, A. M. *Handbook of Polymer–Liquid Interaction Parameters and Solubility Parameters*; CRC Press: Boca Raton, 2018.

(81) Yager, K. G. SciAnalysis. <http://gisaxs.com/index.php/Software> (accessed Aug 15, 2020).

(82) Mouhamad, Y.; Mokarian-Tabari, P.; Clarke, N.; Jones, R. A. L.; Geoghegan, M. Dynamics of Polymer Film Formation during Spin Coating. *J. Appl. Phys.* **2014**, *116*, No. 123513.

(83) Bornside, D. E.; Macosko, C. W.; Scriven, L. E. Spin Coating: One-Dimensional Model. *J. Appl. Phys.* **1989**, *66*, 5185–5193.

(84) Hashimoto, T.; Shibayama, M.; Hawai, H. Ordered Structure in Block Polymer Solutions. 4. Scaling Rules on Size of Fluctuations with Block Molecular Weight, Concentration, and Temperature in Segregation and Homogeneous Regimes. *Macromolecules* **1983**, *16*, 1093–1101.

(85) Arichi, S.; Matsuura, H.; Tanimoto, Y.; Murata, H. Studies of Poly-2-vinylpyridine. II. Solubilities in Various Solvents. *Bull. Chem. Soc. Jpn.* **1966**, *39*, 434–439.

(86) Gu, X.; Gunkel, L.; Hexemer, A.; Russell, T. P. Solvent Vapor Annealing of Block Copolymer Thin Films: Removal of Processing History. *Colloid Polym. Sci.* **2014**, *292*, 1795–1802.

(87) Ruiz, R.; Bosworth, J. K.; Black, C. T. Effect of Structural Anisotropy on the Coarsening Kinetics of Diblock Copolymer Striped Patterns. *Phys. Rev. B* **2008**, *77*, No. 054204.

(88) Majewski, P. W.; Yager, K. G. Millisecond Ordering of Block Copolymer Films via Photothermal Gradients. *ACS Nano* **2015**, *9*, 3896–3906.

(89) Doerk, G. S.; Yager, K. G. Rapid Ordering in “Wet Brush” Block Copolymer/Homopolymer Ternary Blends. *ACS Nano* **2017**, *11*, 12326–12336.

(90) Seguini, G.; Zanenga, F.; Cannetti, G.; Perego, M. Thermodynamics and Ordering Kinetics in Asymmetric PS-*b*-PMMA Block Copolymer Thin Films. *Soft Matter* **2020**, *16*, 5525–5533.

(91) Smilgies, D.-M. Scherrer Grain-Size Analysis Adapted to Grazing-Incidence Scattering with Area Detectors. *J. Appl. Crystallogr.* **2009**, *42*, 1030–1034.

(92) Black, C. T.; Forrey, C.; Yager, K. G. Thickness-Dependence of Block Copolymer Coarsening Kinetics. *Soft Matter* **2017**, *13*, 3275–3283.

(93) Choi, E.; Park, S.; Ahn, H.; Lee, M.; Bang, J.; Lee, B.; Ryu, D. Y. Substrate-Independent Lamellar Orientation in High-Molecular-Weight Polystyrene-*b*-poly(methyl methacrylate) Films: Neutral Solvent Vapor and Thermal Annealing Effect. *Macromolecules* **2014**, *47*, 3969–3977.

(94) Hur, S. M.; Thapar, V.; Ramírez-Hernández, A.; Khaira, G.; Segal-Peretz, T.; Rincon-Delgadillo, P. A.; Li, W.; Müller, M.; Nealey, P. F.; De Pablo, J. J. Molecular Pathways for Defect Annihilation in Directed Self-Assembly. *Proc. Natl. Acad. Sci. U.S.A.* **2015**, *112*, 14144–14149.

(95) Seguini, G.; Zanenga, F.; Laus, M.; Perego, M. Ordering Kinetics in Two-Dimensional Hexagonal Pattern of Cylinder-Forming PS-*b*-PMMA Block Copolymer Thin Films: Dependence on the Segregation Strength. *Phys. Rev. Mater.* **2018**, *2*, No. 055605.

(96) Gopinadhan, M.; Majewski, P. W.; Choo, Y.; Osuji, C. O. Order-Disorder Transition and Alignment Dynamics of a Block Copolymer Under High Magnetic Fields by In Situ X-Ray Scattering. *Phys. Rev. Lett.* **2013**, *110*, No. 078301.

(97) Sepe, A.; Černoch, P.; Štěpánek, P.; Hoppe, E. T.; Papadakis, C. M. Creation of Lateral Structures in Diblock Copolymer Thin Films during Vapor Uptake and Subsequent Drying - Effect of Film Thickness. *Eur. Polym. J.* **2014**, *50*, 87–96.

(98) Peng, Q.; Tseng, Y. C.; Darling, S. B.; Elam, J. W. A Route to Nanoscopic Materials via Sequential Infiltration Synthesis on Block Copolymer Templates. *ACS Nano* **2011**, *5*, 4600–4606.